Geophysical Journal International

Geophys. J. Int. (2010) **182,** 375–388 doi: 10.1111/j.1365-246X.2010.04614.x

Seismic velocity anisotropy of phyllosilicate-rich rocks: characteristics inferred from experimental and crack-model studies of biotite-rich schist

O. Nishizawa[1] and K. Kanagawa[2]

[1]*Institute for Advanced Industrial Science and Technology, Central* 7, 1-1-1 *Higashi, Tsukuba, Ibaraki* 305-8567, *Japan. E-mail: osamu-nishizawa@aist.go.jp*
[2]*Department of Earth Sciences, Chiba University, Chiba* 263-8522, *Japan*

Accepted 2010 April 6. Received 2010 April 6; in original form 2008 September 23

SUMMARY

Seismic velocity anisotropy of biotite schist (30 per cent-mode biotite) was measured under confining pressures up to 150 MPa. The rock shows weak orthotropy which was altered from transverse isotropy (TI) generated by biotite-preferred orientation. The orthotropy was caused by microfolding in the rock. The velocity increase under confining pressure indicates that most crack planes are aligned parallel to the cleavage planes (silicate sheet) of the oriented biotite minerals. The anisotropy of the rock is basically TI due to both the aligned biotite minerals and cracks, which have a common symmetry axis. We found that other sheet silicate-rich rocks have a similar anisotropy with the biotite schist, in which the TI-type anisotropy is characterized by the slow *P*- and *S*-wave velocities along the symmetry axis. This is caused by the preferred orientation of sheet silicate minerals and the extremely slow *P*- and *S*-wave velocities along the axis perpendicular to the silicate sheet compared to the directions along the silicate sheet. When rock contains a large percentage of highly oriented sheet silicates, the fast and slow shear waves exchange their polarities at some off-symmetry axis directions, indicating that the *qS*-wave (quasi-*S* wave) velocity exceeds the *SH*-wave velocity. The phase velocity distribution of *qS* wave shows an asymmetry with respect to the angle from the symmetry axis, which is characterized by a bulge in this distribution located near the symmetric axis. This is inherent to most sheet silicate minerals. When crack density of aligned cracks increases, the *P*-wave velocity along the symmetry axis decreases considerably. The *qS*-wave phase velocity in the off-axis directions also decreases, in accordance with the decrease of the *P* velocity along the symmetry axis. The asymmetry of the *qS*-wave phase velocity distribution increases as the *P*-wave velocity decreases along the symmetry axis. This relationship can be well understood by means of Berryman's extended Thomsen approach.

Key words: Microstructures; Seismic anisotropy; Wave propagation; Acoustic properties.

1 INTRODUCTION

Most studies about rock anisotropy have been concerned with *P*- and *S*-wave velocities in axial directions, which are defined in association with the rock microstructures (Kern & Wenk 1990; Barruol & Mainprice 1993; Kern 1993; Burlini & Kunze 2000), or the *P*-wave velocities over whole solid angles (Pros *et al.* 1998). Recently, studies are more concerned with the *P*- and *S*-wave velocities in off-axis directions [Generally, they are not the true *P* and *S* waves but the quasi-*P* (*qP*) and the quasi-*S* (*qS*) waves] (Jones & Wang 1981; Hornby *et al.* 1994; Johnston & Christensen 1994; Hornby 1998; Jakobsen & Johansen 2000; Takanashi *et al.* 2001; Wang 2002; Sarout & Guéguen 2008).

Some of the sedimentary rocks and metamorphic rocks in the shallow crust generally have planar microstructures. The planar structures often include oriented phyllosilicate (sheet silicate) minerals with their silicate sheets mostly aligned parallel to the structural plane. The previous studies indicate that most of the anisotropic rocks in the shallow crust have slower *P*-wave velocities in the direction normal to the structural plane than in the direction parallel to the plane. This suggests that elastic anisotropy of these rocks is transverse isotropy (TI) or approximated as TI with the symmetry axis perpendicular to the plane. At the same time those rocks have fissility that develops parallel to the structural plane. The fissility suggests that rocks contain thin cracks of which planes are aligned parallel to the isotropic plane of TI symmetry. Aligned cracks bring additional TI-type elastic anisotropy (Anderson *et al.* 1974; Hudson 1981; Nishizawa 1982; Douma 1988; Nishizawa & Yoshino 2001) over the TI anisotropy produced by aligned sheet silicates. In many cases the symmetry axes of both TI are in the same direction. The

elastic anisotropy in sheet silicate-rich rocks is thus controlled by a synergistic effect from the preferred orientations of sheet silicates and cracks.

One of the interesting characteristics in mica-rich rocks or in some shales are that the slow shear waves along the isotropic plane increase at some area in the off-axis directions. The slow shear wave velocity becomes close to or even exceeds another shear wave velocity in the off-axis directions near the symmetry axis (Hornby 1998; Nishizawa & Yoshino 2001; Takanashi *et al.* 2001; Kendall *et al.* 2007; Chesnokov *et al.* 2009). Crossing over of the two shear wave velocity is called a shear wave singularity (Crampin & Yedlin 1981), and it causes problems for seismic ray tracing. Seismologists pay keen attention to the velocity singularity (Vavryčuk 2003). Nishizawa & Yoshino (2001) suggested that the aligned cracks strongly reduce the *P*-wave velocity along the symmetry axis and that the *P*-wave velocity reduction affects the off-axis shear wave velocity distribution. It is important to study how cracks affect seismic velocities in sheet silicate-rich rocks, in terms of numerical modelling and experiments.

Here we investigate velocity anisotropy of a cracked biotite-rich rock that has an orthotropic anisotropy altered from the TI-type anisotropy produced by crystal-preferred orientation (CPO) of biotite. Since cracks in rock close under confining pressure, we can evaluate the crack effect on seismic velocity by measuring velocities under confining pressure. We interpret the velocity data measured under confining pressure, for axial and some of the off-axis directions, by comparing model calculations based on an exact formulation originally shown by Mura (1982). Then we try to draw general features of anisotropy in cracked sheet silicate-rich rocks based on a new formulation derived by Berryman (2008).

2 NUMERICAL MODELLING OF A CRACKED BIOTITE-RICH ROCK

2.1 Inclusion model

To estimate the overall elastic moduli of a cracked medium, we use the Eshelby's (Eshelby 1957) composite medium model consisting of a matrix and inclusions. Let the matrix material have a homogeneous strain, e_{ij}^{A}, or a homogeneous stress field, σ_{ij}^{A}. When an inclusion appears inside the matrix, the composite medium is subjected to an internal stress state. Eshelby (1957) presented an idea, which replaces an inclusion with the matrix material and gives a fictitious stress-free strain inside the inclusion, e_{ij}^{T} (referred to as eigenstrain in Lin & Mura 1973).

Elastic energy change due to inclusions is expressed by e_{ij}^{T}. There are, however, two extreme cases associated with the far field conditions: constant surface displacements and constant external forces (Eshelby 1957; Yamamoto *et al.* 1981; Nishizawa 1982). Since we assume a virtual homogeneous medium, the two cases correspond to equivalent homogeneous strain and equivalent homogeneous stress, respectively. The change of the elastic energy corresponding to the equivalent strain e_{ij}^{A} or stress σ_{ij}^{A} is given by

$$\Delta E = \mp(1/2)\sigma_{ij}^{\mathrm{A}} e_{ij}^{\mathrm{T}} \phi \tag{1}$$

(Eshelby 1957), where the sign $\mp$ corresponds to the two extreme cases at the far field: constant external forces and constant surface displacements, respectively; ϕ is the volume fraction of inclusion; σ_{ij}^{A} is related to homogeneous strain e_{ij}^{A} through the elastic constants of the matrix (c_{ijkl}^{0}) by $\sigma_{ij}^{\mathrm{A}} = c_{ijkl}^{0} e_{kl}^{\mathrm{A}}$.

Let c'_{ijkl} be the elastic constants of the inclusion. The relationship between the stress-free strain e_{ij}^{T} and strain e_{ij}^{A} in the homogeneous matrix is expressed by Eshelby's tensor, S_{ijkl}

$$c_{ijkl}^{0} e_{kl}^{\mathrm{T}} = \Delta c_{ijkl} e_{kl}^{\mathrm{A}} + \Delta c_{ijkl} S_{klmn} e_{mn}^{\mathrm{T}}, \tag{2}$$

where Δc_{ijkl} is the difference between the elastic constants of the matrix and inclusion

$$\Delta c_{ijkl} = c_{ijkl}^{0} - c'_{ijkl}. \tag{3}$$

Eq. (2) shows that the fictitious stress-free strain e_{ij}^{T} can be obtained using e_{ij}^{A}, Eshelby's tensor S_{ijkl}, and the elastic constants of matrix c_{ijkl}^{0}, and inclusion c'_{ijkl}. When the matrix is TI, Eshelby's tensor S_{ijkl} can be calculated by the integrations given by Lin & Mura (1973), which have been employed by several authors (Nishizawa 1982; Douma 1988; Hornby *et al.* 1994). The same problem was recently studied by Markov *et al.* (2005). The Eshelby's tensor in eq. (2) can be calculated, provided that the strain (or stress) inside the inclusion is homogeneous (Nishizawa & Yoshino 2001).

The composite of matrix and inclusions is regarded as an equivalent homogeneous medium and its elastic energy is given by the following equations, corresponding to the conditions in eq. (1):

$$\frac{1}{2} {c_{ijkl}^{*}}^{-1} \sigma_{ij}^{\mathrm{A}} \sigma_{kl}^{\mathrm{A}} = \frac{1}{2} {c_{ijkl}^{0}}^{-1} \sigma_{ij}^{\mathrm{A}} \sigma_{kl}^{\mathrm{A}} + \frac{1}{2} \sigma_{ij}^{\mathrm{A}} e_{ij}^{\mathrm{T}} \phi \ , \tag{4}$$

$$\frac{1}{2} c_{ijkl}^{*} e_{ij}^{\mathrm{A}} e_{kl}^{\mathrm{A}} = \frac{1}{2} c_{ijkl}^{0} e_{ij}^{\mathrm{A}} e_{kl}^{\mathrm{A}} - \frac{1}{2} \sigma_{ij}^{\mathrm{A}} e_{ij}^{\mathrm{T}} \phi, \tag{5}$$

where c_{ijkl}^{*} denotes the elastic constants of the equivalent homogeneous medium, and ${c_{ijkl}^{*}}^{-1}$ and ${c_{ijkl}^{0}}^{-1}$ denote the inverse of the matrices c_{ijkl}^{*} and c_{ijkl}^{0}, respectively. The energy given by eqs (4) or (5) is valid only when ϕ is very small and the inclusions are non-interacting. To obtain the energy change up to the large ϕ, we start with the initial inclusion-free matrix and insert inclusions with a small volume fraction $\Delta\phi$. As illustrated in Fig. 1, we repeat the process by regarding the composite of the previous step as a new equivalent homogeneous matrix material for the next step. This is called the differential equivalent medium (DEM) method or the numerical self consistent (NSC) approach (Yamamoto *et al.* 1981; Le Ravalec & Guéguen 1996a,b). The equations are given by

$$\frac{1}{2} {c_{ijkl}^{*(n)}}^{-1} \sigma_{ij}^{\mathrm{A}(n-1)} \sigma_{ij}^{\mathrm{A}(n-1)} = \frac{1}{2} {c_{ijkl}^{*(n-1)}}^{-1} \sigma_{ij}^{\mathrm{A}(n-1)} \sigma_{kl}^{\mathrm{A}(n-1)} + \frac{1}{2} \sigma_{ij}^{\mathrm{A}(n-1)} e_{ij}^{\mathrm{T}(n-1)} \Delta\phi, \tag{6}$$

$$\frac{1}{2} c_{ijkl}^{*(n)} e_{ij}^{\mathrm{A}(n-1)} e_{ij}^{\mathrm{A}(n-1)} = \frac{1}{2} c_{ijkl}^{*(n-1)} e_{ij}^{\mathrm{A}(n-1)} e_{kl}^{\mathrm{A}(n-1)} - \frac{1}{2} \sigma_{ij}^{\mathrm{A}(n-1)} e_{ij}^{\mathrm{T}(n-1)} \Delta\phi, \tag{7}$$

where $c_{ijkl}^{*(n)}$ and ${c_{ijkl}^{*(n)}}^{-1}$ are the elastic constants and their inverse (compliances) obtained at the nth step of calculation, respectively. The superscripts $(n-1)$ of c_{ijkl}^{*}, e_{ij}^{A}, σ_{ij}^{A} and e_{ij}^{T} denote the values of the $(n-1)$th step. $e_{ij}^{\mathrm{T}(n-1)}$ is obtained from Eshelby's tensor for the effective homogeneous medium of TI anisotropy at the $(n-1)$th step, which has the elastic constants $c_{ijkl}^{*(n-1)}$. Assuming that the composite medium is a new homogeneous matrix material having new elastic constants, we proceed to the next step of the calculation. If both the inclusion and matrix have TI symmetry and the inclusions are aligned to keep their symmetry axes parallel to the symmetry axis of the matrix, the new nominally homogeneous matrix will also be

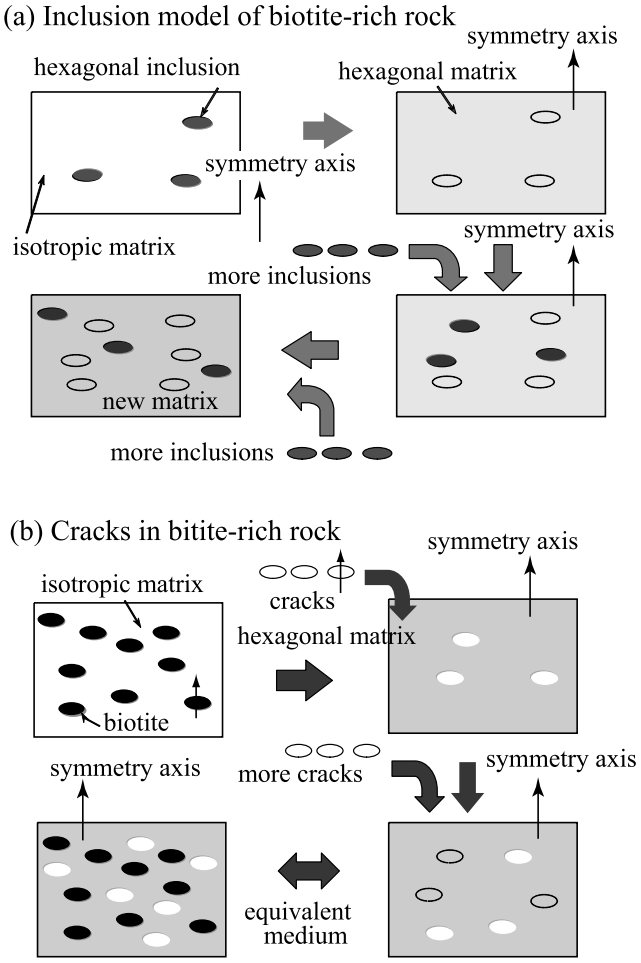

Figure 1. Inclusion models: (a) inclusion model of biotite-rich rock and (b) crack model of biotite-rich rock. (a) A small amount of inclusions with hexagonal symmetry (biotite) are embedded into an isotropic matrix material. → The overall elastic properties of composite medium becomes TI and it is regarded as a new homogeneous TI material. Inclusions are shown by dotted line. → Again, more inclusions are embedded into the TI matrix. → The process is repeated until the biotite volume fraction becomes equal to the expected value. (b) The biotite-rich rock is assumed as a composite material having aligned biotite and isotropic matrix. → The rock is assumed to be an equivalent TI homogeneous material. Aligned fluid-filled cracks are embedded in the matrix. This keeps TI symmetry. → The cracked rock is assumed as a new TI homogeneous material, and more aligned cracks are embedded in to the matrix. ↔ The material is equivalent to the cracked biotite-rich rock. The process of calculation is same as the biotite inclusion model in (a) except that the initial matrix is TI, not isotropic.

TI. The above two extreme cases overestimate or underestimate the value of the real energy change, and the elastic constants calculated from eqs (6) and (7) give the lower and upper bounds, respectively (Hill 1952). We use an average of the elastic constants obtained from eqs (6) and (7) for this study as suggested by Yamamoto *et al.* (1981).

2.2 Calculating elastic constants of biotite-rich rock

We consider a biotite-rich rock consisting of an isotropic matrix and 30 per cent volume fraction of biotite. We assume the elastic constants of the isotropic matrix as $\lambda = \mu = 35$ GPa, which are plausible values of the matrix material forming an aggregate

Table 1. Elastic constants of biotite (GPa).

	C_{11}	C_{33}	C_{44}	C_{66}	C_{13}
Biotite	186.0	54.0	5.8	76.8	11.6

Table 2. Elastic constants of biotite-rich rock model (30 per cent biotite, GPa).

	C_{11}	C_{33}	C_{44}	C_{66}	C_{13}
Crack-free rock	126.6	81.9	15.8	47.0	24.4

of quartz and feldspar group minerals that are common in ordinary biotite-rich rocks. Biotite belongs to the monoclinic space group, but elastically it can be regarded as hexagonal for which the symmetry axis is perpendicular to the silicate sheet (Vaughan & Guggenheim 1986). We used the elastic constants given in Table 1 (Aleksandrov & Ryzhova 1961). Hereafter, the reduced Voigt notation C_{ij} ($i, j =$ 1–6) is used for denoting the measured and calculated elastic constants, instead of c_{ijkl} in the previous theoretical formulations. In TI media, there are five independent values out of 12 non-zero matrix elements, $C_{11}, C_{33}, C_{44}, C_{66}$ and C_{13}, with the relationship $C_{12} = C_{11} - 2C_{66}$.

When the symmetry axes of hexagonal crystals align in the same direction, we can calculate the overall elastic properties by employing the method described in the previous section. Fig. 1(a) illustrates the process for calculating elastic constants of the rock having aligned biotite minerals. Controlled by the cleavage plane parallel to the silicate sheet, biotite minerals usually appear as thin crystals, and mineral shapes are approximated as oblate spheroids described by the major axis, a, and the minor axis, c. Since the present method considers static deformation, the size of inclusion does not affect overall elastic properties. Only the aspect ratio α ($= c/a$) of inclusions affects the effective elastic properties.

Nishizawa & Yoshino (2001) pointed out that the crystal shape of biotite affects the overall S-wave anisotropy of biotite-rich rocks. However the crystal-shape effect on the overall S-wave velocity is significant only when α of biotite crystal is $1/20 \leq \alpha \leq 1/10$. Taking the biotite shapes in the typical biotite-rich rocks into account (Takanashi *et al.* 2001), we assume the aspect ratio of biotite crystal 1/20. Less than this value, they do not severely affect the velocity anisotropy in rocks. The values in Table 2 are obtained for a rock containing 30 per cent biotite by using the method described by Nishizawa & Yoshino (2001). These are used as the elastic constants of the initial matrix of aligned crack models.

We then also assume that the initial crack-free biotite-rich rock is a homogeneous TI material and inserts aligned microcracks into the matrix. Fig. 1(b) illustrates the process for inserting aligned cracks into the TI matrix. In each step of the calculation, we obtain two elastic constants, corresponding to the eqs (6) and (7). The difference between the two elastic constants becomes large as the difference of elastic constants between inclusion and matrix becomes large. The difference is also controlled by the crack aspect ratio and the step volume fraction $\Delta\phi$. However, crack density is the unique parameter that includes the effects of both crack shape and crack volume fraction. Crack density is proportional to the value ϕ/α. We selected the step volume fraction $\Delta\phi$ so as to keep small values for $\Delta\phi/\alpha$. We calculate averages of the two elastic constants obtained from eqs (6) and (7).

2.3 Seismic velocities in TI media

Seismic velocities of an equivalent homogeneous medium with elastic constants $c^{*(n)}_{ijkl}$ are given by the wave equation

$$\rho \frac{\partial^2 u_i}{\partial t^2} = c^{*(n)}_{ijkl} \frac{\partial^2 u_k}{\partial x_j \partial x_l}, \tag{8}$$

where ρ is the rock density and u_i is the ith component of the wave particle motion. The equation can be solved for the plane wave propagating with the wavenumber (q_1, q_2, q_3), where q_i denotes the x_i component of the wave vector $\boldsymbol{q}$. The relationship between ω and $\boldsymbol{q}$ is given by the Christoffel equation (Landau & Lifshitz 1959)

$$\left| \rho\omega^2 \delta_{ik} - c^{*(n)}_{ijkl} q_j q_l \right| = 0. \tag{9}$$

Phase velocities are obtained by $\omega/|\boldsymbol{q}|$ for the three independent solutions. The corresponding displacement vector gives the polarization direction of seismic waves (Carcione 2007).

In what follows, we deal with only TI media. Among the three phase velocities calculated from eq. (9), the polarization direction of the fastest wave generally deviates from the propagation direction except when the wave propagates along the symmetry axis or on the isotropic plane. This wave is referred to as the quasi-*P* wave, *qP*, to distinguish from the true *P* wave of which polarization is directed to the propagation direction. The polarization of one of the *S* waves generally deviates from the true *S*-wave polarization that is in the plane perpendicular to the propagation direction. The wave is referred to as the quasi-*S* wave, *qS*. Another *S* wave is the true *S* wave with polarization parallel to the isotropic plane and perpendicular to the propagation direction. When waves propagate along the symmetry axis or on the isotropic plane, the two shear waves are the true *S* waves polarized perpendicular to the propagation direction. Along the symmetry axis their velocities are equal but they are different in the isotropic plane. The phase velocities of *qS* and *SH* waves are generally different in diagonal directions. Each phase velocity depends only on the angle measured from the symmetry axis, θ.

In TI media there are only five independent elastic constants, and eq. (9) can be described in explicit form by using C_{ij}. The phase velocities of *qP* and *qS* waves, V_{qP} and V_{qS}, are given by the following equations (Mavko *et al.* 1998):

$$V_{qP} = \frac{\left[C_{11}\sin^2\theta + C_{33}\cos^2\theta + C_{44} + \sqrt{M(\theta)} \right]^{1/2}}{(2\rho)^{1/2}}, \tag{10}$$

$$V_{qS} = \frac{\left[C_{11}\sin^2\theta + C_{33}\cos^2\theta + C_{44} - \sqrt{M(\theta)} \right]^{1/2}}{(2\rho)^{1/2}}, \tag{11}$$

where $M(\theta)$ is

$$M(\theta) = \left[(C_{11} - C_{44})\sin^2\theta - (C_{33} - C_{44})\cos^2\theta \right]^2 + 4(C_{13} + C_{44})^2 \sin^2\theta \cos^2\theta . \tag{12}$$

The phase velocity of *SH* wave, V_{SH} is given by

$$V_{SH} = \left[(C_{66}\sin^2\theta + C_{44}\cos^2\theta)/\rho \right]^{1/2}. \tag{13}$$

2.4 Thomsen's approximation and extended Thomsen formulae for TI media

For interpreting field observations, it will be useful to describe phase velocities as simple functions of θ. Thomsen (1986) derived formulae that approximate the angular dependence of phase velocities, $V_{qP}(\theta)$, $V_{qS}(\theta)$ and $V_{SH}(\theta)$ for weak anisotropy. He derived anisotropic parameters ε, δ and γ, (and a non-independent parameter η) referred to as Thomsen's anisotropic parameters. ε and γ are obtained from the axial *P*- and *S*-wave velocities $V_P(0)$, $V_P(\pi/2)$, $V_S(0)$ and $V_S(\pi/2)$, δ is obtained from one of the off-axis *qP* or *qS* velocity.

In Thomsen's approximation, phase velocities are expressed as

$$V_{qP}(\theta) = V_P(0)(1 + \delta \sin^2\theta \cos^2\theta + \varepsilon \sin^4\theta), \tag{14}$$

$$V_{qS}(\theta) = V_S(0)(1 + \eta \sin^2\theta \cos^2\theta), \tag{15}$$

$$V_{SH}(\theta) = V_S(0)(1 + \gamma \sin^2\theta), \tag{16}$$

δ becomes precise when using the *qP* velocity near the diagonal direction ($\theta = \pi/4$) because $\sin^2\theta\cos^2\theta$ takes the maximum value in eq. (14). There are relationships between anisotropic parameters, elastic constants and the velocity values along $\theta = 0, \pi/2$ and $\pi/4$.

$$\varepsilon = \frac{C_{11} - C_{33}}{2C_{33}} \approx \frac{V_P(\pi/2) - V_P(0)}{V_P(0)}, \tag{17}$$

$$\gamma = \frac{C_{66} - C_{44}}{2C_{44}} \approx \frac{V_{SH}(\pi/2) - V_{SH}(0)}{V_{SH}(0)}, \tag{18}$$

$$\delta = \frac{(C_{13} + C_{44})^2 - (C_{33} - C_{44})^2}{2C_{33}(C_{33} - C_{44})} \approx 4\left[\frac{V_{qP}(\pi/4)}{V_P(0)} - 1 \right] - \left[\frac{V_P(\pi/2)}{V_P(0)} - 1 \right], \tag{19}$$

η in eq. (15) is given by

$$\eta = \left[\frac{V_P(0)}{V_S(0)} \right]^2 (\varepsilon - \delta), \tag{20}$$

where η controls the magnitude of V_{qS} in off-axis directions. V_{qS} takes an extreme value at $\theta = \pi/4$ (eq. 15).

Recently, Berryman (2008) derived extended Thomsen formulae applicable for strong anisotropy. The major extension is that the new approximation removes an implicit restriction of the diagonal symmetry of the angular distributions of V_{qS}, which is caused by the extreme values at $\theta = \pi/4$.

The exact velocities of *qP* and *qS* are given by eqs (10) and (11). We denote the angle of the extreme value of $M(\theta)$ by θ_m.

$$\tan^2\theta_m = \frac{C_{33} - C_{44}}{C_{11} - C_{44}}. \tag{21}$$

V_{qP} and V_{qS} are approximated by using θ_m as

$$V_{qP}(\theta) = V_P(0)\left[1 + \varepsilon \sin^2\theta - (\epsilon - \delta)\frac{2\sin^2\theta_m \sin^2\theta\cos^2\theta}{1 - \cos 2\theta_m \cos 2\theta} \right] \tag{22}$$

and

$$V_{qS} = V_S(0)(1 + \eta)\left[\frac{2\sin^2\theta_m \sin^2\theta\cos^2\theta}{1 - \cos 2\theta_m \cos 2\theta} \right]. \tag{23}$$

We now examine the applicability of the Thomsen's and the extended Thomsen's approximation for biotite-rich rocks.

2.5 Phase velocities of the biotite-rich rock model

For calculating the phase velocities in the biotite-rich rock, we assume the rock density 2.75×10^3 kg m^{-3}. The value is equal to the density of biotite schist measured in the present experiment (ST-3 of Takanashi *et al.* 2001). The bulk modulus of the crack-filling fluid controls velocity anisotropy. Fluid bulk modulus differs by orders of magnitude between liquid and gas. We assumed the fluid bulk modulus $K_f = 0.01$ and 1 GPa for gas and liquid, respectively, corresponding to typical cases of gas-filled and liquid-filled cracks in underground conditions.

To describe the relationship between seismic velocities and cracks, crack density is conventionally used (O'Connell & Budiansky 1974). Crack density corresponds to a population of cracks with specific aspect ratio, and shows the combined effect of crack volume and crack shape on seismic velocities. The crack density ϵ is given by each crack porosity ϕ_i (the volume fraction of crack) and its crack aspect ratio α_i as

$$\epsilon = \sum_{i=1}^{N} \gamma_i \phi_i / \alpha_i, \tag{24}$$

where γ_i is the geometrical shape factor for each open crack, and N is the total number of cracks. For oblate spheroidal cracks $\gamma_i = 3/4\pi$. When crack closes under external forces, ϕ_i becomes zero. Crack density decreases as cracks close, then velocities increase. Velocity change can be described as a function of crack density (O'Connell & Budiansky 1974; Soga *et al.* 1978). It is enough to calculate wave velocities for a representative crack shape as a function of crack density because crack density is the unique parameter that controls the velocity in a cracked medium.

In the phase-velocity calculations of Fig. 2, we adopted a single value of 0.0025 (1/400) for crack aspect ratio and show results for different crack densities and different fluid bulk moduli. Figs 2(a)–(d) show angular distributions of phase velocity plotted on one of the quadrants formed by the symmetry axis and the isotropic plane of TI symmetry (hereafter simply referred to as the quadrant). The fluid bulk modulus K_f is assumed as 0.01 GPa. The thick solid curves correspond to the crack densities 0.02 and 0.06, respectively. The thin solid curves show velocity distributions in the crack-free state to show the velocity change due to cracks. Figs 2(a) and (b) show V_{qP}, and Figs 2(c) and (d) show both V_{qS} and V_{SH}. The right- and left-hand panels correspond to crack densities 0.02 and 0.06, respectively. Figs 2(e)–(h) show phase velocities for another typical value of fluid bulk modulus $K_f = 1$ GPa. The panels in the upper and lower rows and the left- and right-hand columns correspond to the same conditions as in Figs 2(a)–(d).

The angular dependence of phase velocity for the model matrix (thin solid curves) are characterized by inflected curves in the V_{qP} distribution, and the diagonal bulge in the V_{qS} distribution. The diagonal bulge shrinks as the crack density increases (*cf.* Figs 2c and d), or the fluid bulk modulus becomes smaller (*cf.* Figs 2d and h). When fluid bulk modulus is small, cracks have more effects on the *P*-wave velocity anisotropy, that is the velocity difference between the symmetry axis and the isotropic plane, compared to the *S*-wave anisotropy. Increase of crack density reduces the off-axis *qS*-wave velocities. The reduction is more pronounced when compared to the reduction of the *qS*-wave velocity along the symmetry axis and the isotropic plane for the case $K_f = 0.01$ GPa. This moves the crossover point of the V_{qS} and V_{SH} distribution curves closer to the symmetric axis (typically in Fig. 2d). The difference between V_{SH} and V_{qS} in the same direction is referred to as the shear wave splitting. Since the velocity of the *SH* wave is insensitive to crack density, the shear wave splitting is mainly affected by the angular distribution of V_{qS}. The bulge in the V_{qS} distribution shrinks with increasing crack density. The shrinkage affects the shear wave splitting. Thus shear wave splitting is sensitive to crack density at some area of the off-axis directions. With increasing crack density, a reversal of the fast and slow shear wave polarization may occur in a certain range of θ when fluid bulk modulus (K_f) is small.

Thomsen's and the extended Thomsen's approximations are also plotted for all the cases. There are considerable differences in Thomsen's parameters defined by elastic constants and those calculated from velocities by using eqs (17)–(19). We use axial velocities for calculating ε and γ. δ shows considerable difference between the two values: from elastic constants and from $V_{qP}(\pi/4)$. We use δ_M that is determined from the elastic constants (moduli). In Figs 2(a)–(h), Thomsen's approximation and the extended Thomsen's approximation are plotted as the dotted curves and the break curves, respectively. For V_{qP}, the extended Thomsen's approximation shows better fits to the velocity distribution curves than Thomsen's approximation, even for higher crack density and small fluid bulk modulus. For V_{SH}, Thomsen's approximation and the extended Thomsen's approximation are the same. The approximation fits well to the *SH* velocity distribution curves, and the velocities are unaffected by the crack density and the fluid bulk modulus. Thomsen's approximation by using δ_M overestimates the actual *qS*-wave velocity. The extended Thomsen's approximation always underestimates the maximum values of V_{qS}.

3 LABORATORY VELOCITY MEASUREMENTS OF BIOTITE SCHIST

3.1 Velocities under 150 MPa confining pressure

To examine crack effects on seismic velocities in the biotite-rich rock model presented above, we made laboratory velocity measurements of Hidaka biotite schist under confining pressures up to 150 MPa. The rock was sampled from Hidaka metamorphic belt, Hokkaido, Japan (the sample ST-3 in Takanashi *et al.* 2001). The rock shows well-developed foliation plane and lineations in the foliation plane. The cleavage planes of biotite crystals are mostly aligned parallel to the foliation plane (fig. 2 and fig. 4 of Takanashi *et al.* 2001). Rock density, CPO data and seismic velocity anisotropy at the confining pressure 150 MPa are presented in Takanashi *et al.* (2001).

Anisotropy of the rock is described with respect to the foliation plane. We select x_3-axis perpendicular to the foliation plane, and x_1- and x_2-axes parallel and perpendicular to the lineation, respectively. *P*- and two polarized *S*-wave velocities were measured along the three axes and in diagonal directions in the x_1x_3- and x_2x_3-planes. The polarization directions of *S* waves are parallel and perpendicular to propagation directions. Figs 3(a-1) and (a-2) show the microstructure and the biotite *c*-axis distribution of the rock. Velocities were measured by the pulse transmission method. We used piezo-electric transducers of compression and shear modes with 5-mm-diameter disc and 6 mm × 3 mm rectangular plate, for measuring *P*- (*qP*) and *S*-wave (*qS*) velocities, respectively. The travel distances of elastic waves are 50–80 mm. In this distance range, elastic waves are approximated as plane waves and measured velocities are almost equal to the phase velocities (Dellinger & Vernik 1994). Velocities at the confining pressure 150 MPa are shown in Fig. 3(b). The two panels in Fig. 3(c) show angular velocity distributions in the two quadrant sections, x_1x_3 and x_2x_3. The distributions

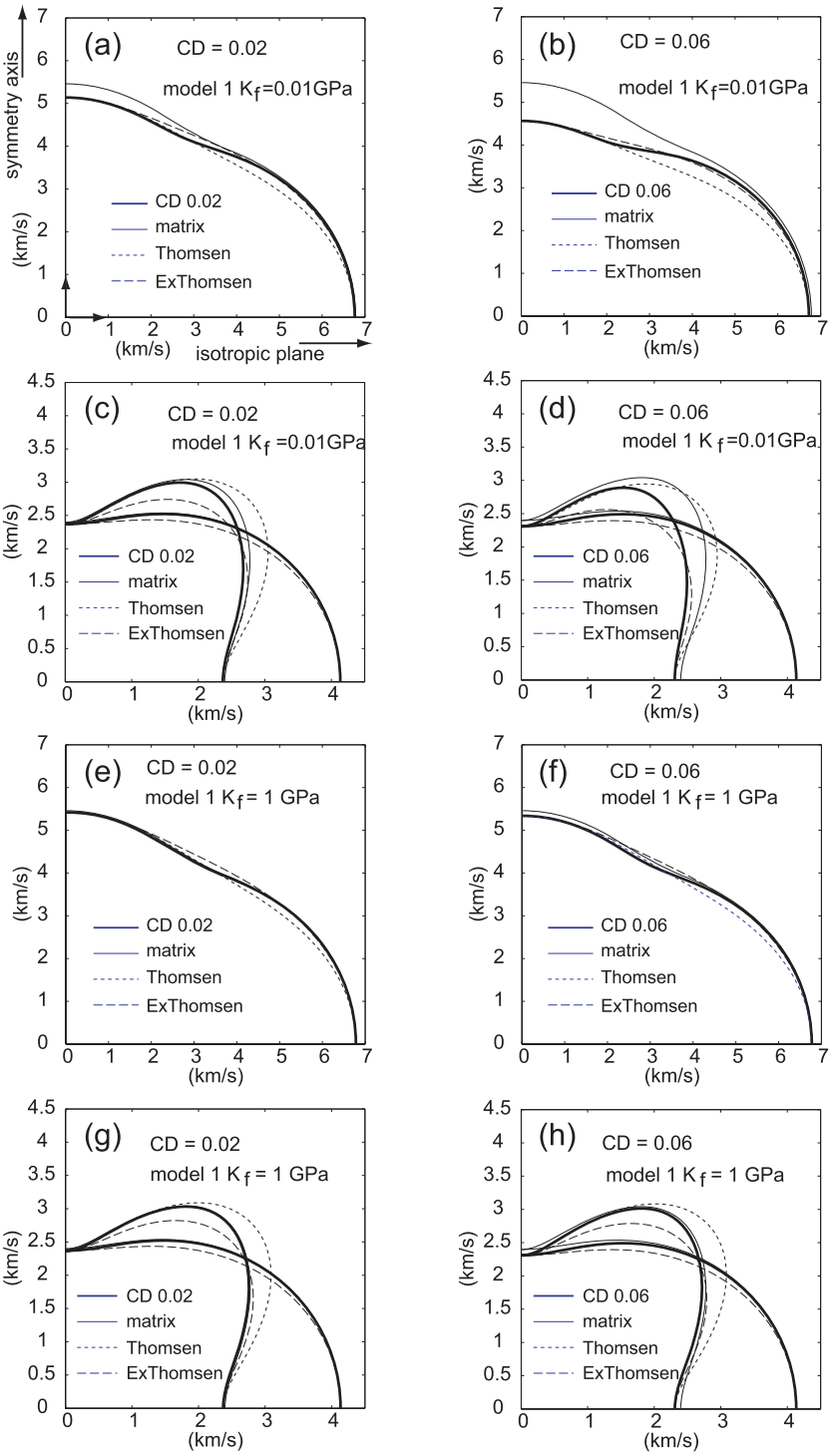

Figure 2. Angular phase-velocity distributions for *qP*, *qS* and *SH* waves. Values are plotted on one of the quadrants formed by the symmetry axis (vertical direction) and isotropic plane (horizontal direction). The rock contains 30 per cent volume fraction of biotite. Crack aspect ratio is 0.0025 (1/400) for all calculations. The fluid bulk modulus for (a)–(d) is 0.01 GPa, and for (e)–(h), 1 GPa. The left and right columns correspond to low (0.02) and high (0.06) crack densities (CD). The phase velocities for the aligned crack cases are shown by thick curves. Crack-free states and approximations by Thomsen and the extended Thomsen are shown by thin, dotted and dashed curves, respectively.

are calculated from the velocity data in each plane at 150 MPa. Those velocity distributions will be discussed in the succeeding subsections.

Axial velocities under 150 MPa confining pressures and the biotite CPO data indicate that the velocity anisotropy comes from preferred orientation of biotite minerals. Biotite minerals basically align their cleavage plane parallel to the foliation plane. This produces TI-type seismic velocity anisotropy. In the x_2x_3 section, the cleavage planes of biotite show slight misalignments from the foliation plane (Takanashi *et al.* 2001), forming microscale folding accompanied by crenulation cleavage of the rock. The misalignments of biotite cleavage planes and crack planes from the foliation

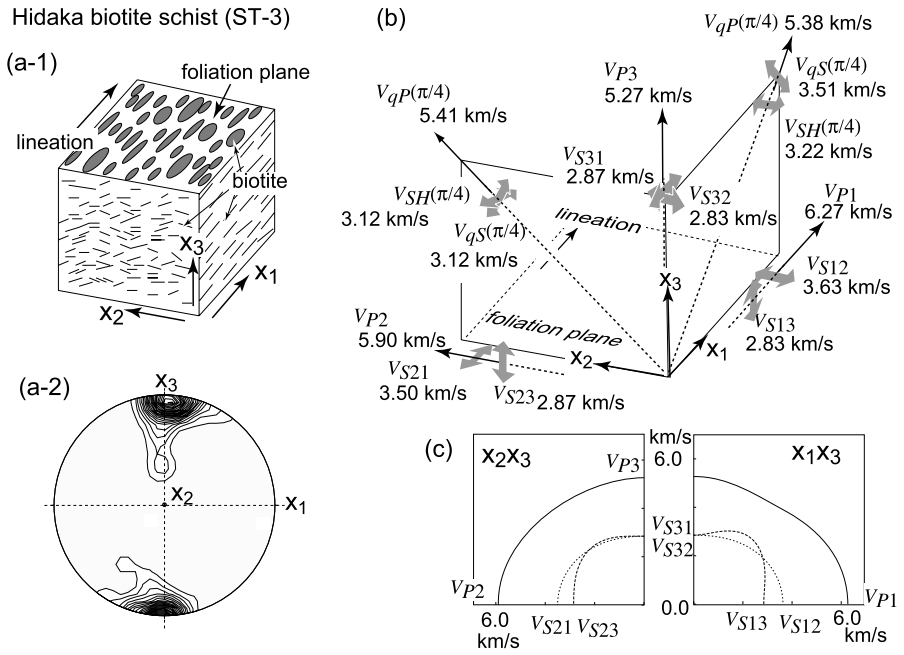

Figure 3. (a-1) A sketch of the microstructure. (a-2) The biotite *c*-axis distribution of biotite schist. The contour is an arbitrary scale modified from Takanashi *et al.* (2001). (b) 150-MPa confining-pressure velocities along the axial and the diagonal directions in the x_2x_3- and x_1x_3-planes. The axes are selected in reference to the foliation plane and the direction of lineation. x_3-axis is perpendicular to the foliation plane, and x_1- and x_2-axes are parallel and perpendicular to the lineation, respectively. Two orthogonally polarized shear waves show different velocities in the diagonal directions of the x_1x_3-plane, whereas the two shear wave velocities are equal in the diagonal directions of the x_2x_3-plane. Approximation is made by assuming the x_3-axis as the symmetry axis and the velocities in the x_1x_3-planes represents the velocities in TI anisotropy.

plane alter the velocity anisotropy from TI to orthotropic symmetry. To see the effect of cracks on seismic velocity, we approximate the rock anisotropy by a combination of the two TI anisotropies seen in the x_1x_3-plane and the x_2x_3-plane. This kind of simplification was employed in the field seismic data analysis for orthotropic anisotropy (Tsvankin 1997).

The *P*-wave velocity in the x_2 direction is slower than that in the x_1 direction. This is due to the misalignments of biotite sheets and cracks from the foliation plane. In the x_1x_3-plane, the fast shear wave is polarized in the plane including the symmetry axis in the direction $\theta = \pi/4$. The detected fast shear wave is considered as the *qS* wave. A crossover between the V_{SH} and V_{qS} distribution appears in the x_1x_3-plane because V_{SH} exceeds V_{qS} in the x_1-axis. The V_{qS} distribution forms a bulge in the x_1x_3-plane (Fig. 14 of Takanashi *et al.* 2001), similar to the phase velocity distribution of Fig. 2. On the other hand, the two polarized shear wave velocities along the direction $\theta = \pi/4$ are almost equal. This suggests that the bulge of the *qS* phase-velocity distribution in the x_2x_3-plane is very small. The velocities in the x_1x_3-plane under 150 MPa show striking similarities to the velocities in the biotite-rich rock model presented in the previous section.

3.2 Velocity increase from atmospheric pressure to 150 MPa

Fig. 4(a) shows the pressure dependence of the axial velocities and the velocities along the $\theta = \pi/4$ direction in the x_1x_3- and x_2x_3-planes. The *P*-wave velocity perpendicular to the foliation plane, V_{P3}, increases by about 1.5 km s^{-1} (3.78–5.27 km s^{-1}) as the confining pressure increases from atmospheric pressure to 150 MPa, whereas the *P*-wave velocity in the x_1 (lineation) direction, V_{P1}, increases only by 0.5 km s^{-1} (5.74–6.27 km s^{-1}) in the same pressure range. The velocity in the x_2 direction increases by 0.7 km s^{-1} in this pressure range. Both in the x_1x_3- and x_2x_3-planes, the *qP*-wave velocities along $\theta = \pi/4$, $V_{qP}(\pi/4)$, increases with increasing the confining pressure. $V_{qP}(\pi/4)$ becomes close to V_{P3} at 150 MPa.

The axial *S*-wave velocities are denoted by V_{Sij} where *i* and *j* correspond to propagation and polarization directions, x_i- and x_j-axis directions, respectively. *S*-wave velocities show only a small increase compared to *P*-wave velocities except for $V_{qS}(\pi/4)$ in the x_1x_3-plane. The differences between V_{S12} and V_{S13}, and V_{S21} and V_{S23} show the intensity of shear wave splitting in the x_1 and x_2 axial directions, respectively. Those differences do not show remarkable changes with increasing confining pressure. However, in the direction $\theta = \pi/4$ in the x_1x_3-plane, the difference between $V_{qS}(\pi/4)$ and $V_{SH}(\pi/4)$, does change significantly with increasing confining pressure. In contrast, in the direction $\theta = \pi/4$ in the x_2x_3-plane, $V_{qS}(\pi/4)$ and $V_{SH}(\pi/4)$ are almost equal.

4 DISCUSSION

4.1 Closure of cracks under confining pressure

We interpret the pressure dependence of velocity in Hidaka biotite schist by assuming aligned cracks in a TI matrix. Because more cracks close as the confining pressure increases, the increase of seismic velocity under confining pressure results from the decrease of crack density. In isotropic materials, the following equation gives the crack-closing pressure (p_c) for the cracks having the aspect ratio α (Walsh 1965; Simmons *et al.* 1974)

$$p_c = \frac{\pi E \alpha}{4(1-\nu^2)}, \tag{25}$$

where E and ν are the Young's modulus and the Poisson's ratio of the matrix material, respectively. Since Poisson's ratio takes the value

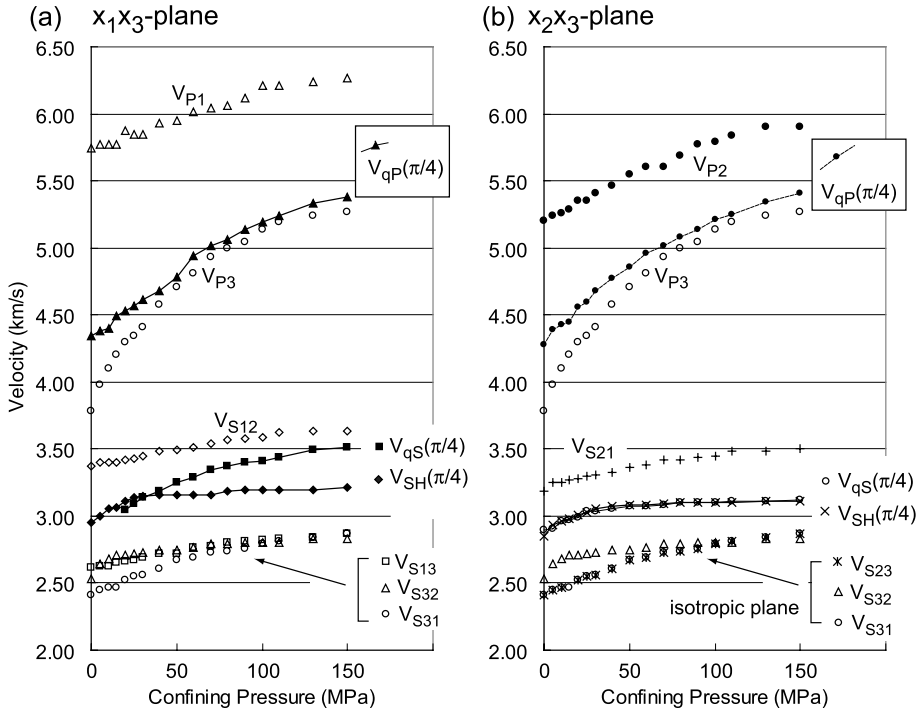

Figure 4. Seismic velocities in the Hidaka biotite schist as functions of confining pressure. (a) Velocities in the x_1x_3-plane. (b) Velocities in the x_2x_3-plane.

between 0.2 and 0.3 for the most of crystalline rocks, eq. (25) gives an approximation that p_c is nearly equal to $E\alpha$. The relationship will hold for the present anisotropic rock matrix, giving only a small change for p_c since the effective E is almost the same for the present aligned crack case.

If we tentatively assume that E is 60 GPa (a plausible value for crystalline rocks), the cracks with aspect ratio less than about 1/400 will close at 150 MPa. Cracks with the larger aspect ratios still exist above 150 MPa. Technically, the rock is not a crack-free material under 150 MPa, but we regard the rock at 150 MPa as an equivalent homogeneous material even if the rock actually includes cracks and voids. Then we can calculate elastic constants of the rock below this pressure by inserting cracks into this nominally homogeneous matrix.

4.2 TI velocity anisotropy in the x_1x_3- and x_2x_3-planes

Schist often tends to split along their foliation plane. This indicates that microcracks mostly distribute along the foliation plane with crack planes almost parallel to the foliation plane. To interpret elastic wave velocities under confining pressure, it will be reasonable to apply the aligned crack model as the first approximation.

The experimental velocity data show different velocity increases between x_1x_3- and x_2x_3-planes. The differences are induced by microfolding seen in the x_2x_3-plane, which induce an orthotropy in an original TI-type anisotropy due to CPO of biotite. The velocities under 150 MPa confining pressure indicate two TI velocity anisotropies that are similar to the biotite-rich rock.

Although the schist shows an orthotropic velocity anisotropy, we consider two different TI anisotropies in the x_1x_3- and x_2x_3-planes. The difference is induced by the differences in biotite-preferred orientations. We try to interpret velocities under confining pressure in the two planes independently. We obtain the following elastic constants for C_{11}, C_{33}, C_{44} and C_{66} for the x_1x_3- and x_2x_3-planes of Hidaka biotite schist. We adopt the measured density, 2.75×10^3 kg m^{-3} (ST-3 in Takanashi *et al.* 2001). C_{13} was estimated from the measured $V_{qP}(\pi/4)$ and other four elastic constants. Table 3 shows the estimated C_{ij} of Hidaka biotite schist in the x_1x_3- and x_2x_3-planes at 150 MPa where the rock is nominally crack-free. We calculate velocities in each direction as functions of crack density by using those elastic constants.

Table 3. C_{ij} for Hidaka biotite schist (GPa).

	C_{11}	C_{33}	C_{44}	C_{66}	C_{13}
x_1x_3-plane	108.1	76.35	22.33	36.22	19.35
x_2x_3-plane	95.70	76.35	22.33	33.68	29.35

4.3 Phase velocity as a function of crack density

We calculate velocities by using the same method as for the previous biotite-rich rock model by considering the schist as a TI matrix. Calculated velocities in each measured direction are shown in Figs 5(a)–(c) as functions of crack density. Figs 5(a) and (b) show the velocities in the assumed TI media for the x_1x_3- and x_2x_3-planes, respectively. Fig. 5(c) shows the same relationship for the biotite-rich rock model I in Table 2. The horizontal axis scales are reversed in accordance with the inverse proportionality between crack-closing pressure and the crack density as indicated by eqs (24) and (25).

The observed velocities increase with increasing confining pressure. Because velocities under confining pressure do not show the quantitative relationship between velocity and crack density, the two horizontal axes in Figs 4 and 5 cannot be compared directly. The total crack density is given by the summation of the crack densities of different aspect ratio cracks as given by eq. (24). Under low confining pressures, cracks with smaller aspect ratios are preferentially closed. Crack density decreases because the smaller α

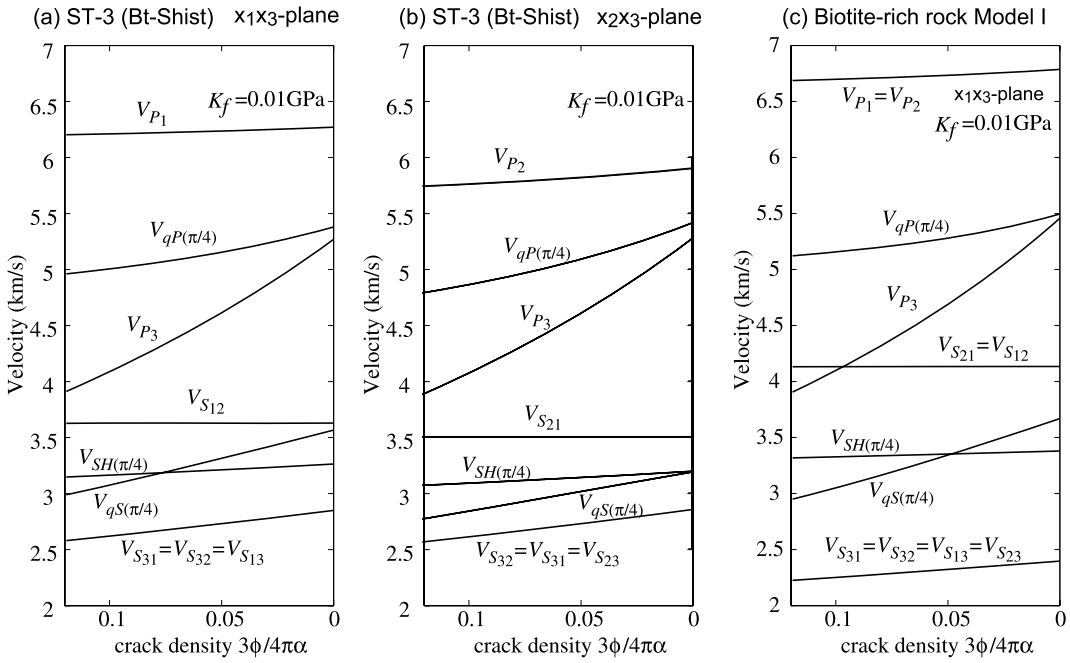

Figure 5. Seismic velocities in the three models as functions of pressure: (a) aligned crack model estimated from the velocities at 150 MPa in the x_1x_3-plane; (b) aligned crack model estimated from the velocities at 150 MPa in the x_2x_3-plane; (c) biotite-rich rock model I.

values in the denominator in eq. (24) are dropped out. To obtain the quantitative relationships, we need to know the distribution of the crack aspect-ratio population (Simmons *et al.* 1974). We do not have the data about crack aspect-ratio distribution. But if we assume that the crack porosity is of the same order for different aspect ratios, velocities are more affected in the low confining pressure range because of closure of low aspect-ratio cracks. If the crack density rapidly decreases with increasing confining pressure at the low confining pressures, the rapid velocity increases in the low confining pressure range in Fig. 4 will correspond to rapid decrease of crack density due to closing of thin cracks. Because *P*-wave velocity is more sensitive to the crack density, increase of *P*- (or *qP*-) wave velocity is more pronounced than *S*-wave velocities.

Even considering closure of the aligned thin cracks, there still remain discrepancies in the velocity increase at the low confining pressure range. V_{P1} and V_{P2} increase more than the expected values in Fig. 5. We have to consider other crack orientations. Nur & Simmons (1969) showed that closure of randomly oriented thin cracks brings considerable velocity increase in crystalline rocks at the low confining pressure range. Increase in V_{P1} and V_{P2} at the low pressure range suggests that a certain population of randomly oriented thin cracks could be superposed to the population of aligned cracks. In addition to the aligned and random crack orientations, another population of crack orientations will be associated with the microfolding, where crack planes are slightly slanted from the x_1x_2-plane. Those slanted cracks would affect the axial velocities in a different manner as shown in Fig. 6.

When *P* and *SH* waves are propagating parallel to crack planes, their velocities are little affected by cracks. For the slanted cracks in Fig. 6, V_{P1} propagates parallel to the crack plane. In this case, the *P* wave does not pass through the crack plane. On the other hand, V_{P2} is affected strongly by the slanted cracks because it passes through the crack planes. V_{P3} propagates normal to the crack planes of aligned cracks. Slanted cracks slightly change the incident angle of V_{P3}, but this will have little effect on velocity. Slanted biotite sheets will have slight effect on V_{P3} because V_{P3} increases in the off-axial directions around the symmetry axis as shown in Fig. 2.

V_{S12} and V_{S21} are slightly affected by the slanted cracks. V_{S12} propagates parallel to the slanted crack plane but its polarization is slightly inclined with respect to the crack plane. On the other hand, the *S*21 wave propagates through the slanted crack plane with a small angle from the crack plane. The polarization direction of the *S*12 wave shows slight deviations from the slanted crack plane and the major vibration direction is still parallel to crack plane. *S*21 wave propagates through the slanted crack plane and is more affected by slanted cracks than *S*12 wave. V_{S21} is therefore more affected by cracks than V_{S12}.

4.4 Angular velocity distributions

Ignoring the small differences caused by the cracks with normals directed off the x_3-axis, the relationship between calculated velocities and crack density will correlate to the pressure dependence of the measured velocity. For example, in Fig. 4(a) V_{P3} becomes close to $V_{qP}(\pi/4)$ as confining pressure increases. This is similar to the large increase of V_{P3} and rather small increase in $V_{qP}(\pi/4)$ as shown in Fig. 2(b) with decreasing crack density. A crossover of the two shear wave velocities in the diagonal direction, $V_{SH}(\pi/4)$ and $V_{qS}(\pi/4)$, appears in Fig. 4(a). $V_{qS}(\pi/4)$ becomes larger than $V_{SH}(\pi/4)$ as crack density decreases. This is similar to the change in the *qS*- and *SH*-wave velocity in off-axis directions with decreasing crack density, as shown in the biotite-rich rock model in Fig. 2(d). We conclude that the experimental results can be basically explained by crack models having aligned thin cracks in the biotite-rich rock matrix having a TI-type anisotropy.

We examine velocity anisotropy of cracked biotite-rich rocks in more detail, by plotting phase velocity in all directions. Figs 7(a)–(d) show phase velocity of the biotite schist calculated from the elastic constants in Table 3. As crack density increases, the anisotropy in *P* wave is more enhanced; the phase velocity surface of *qP* wave shows a flat-bottomed pan shape, indicating that the *qP*-wave

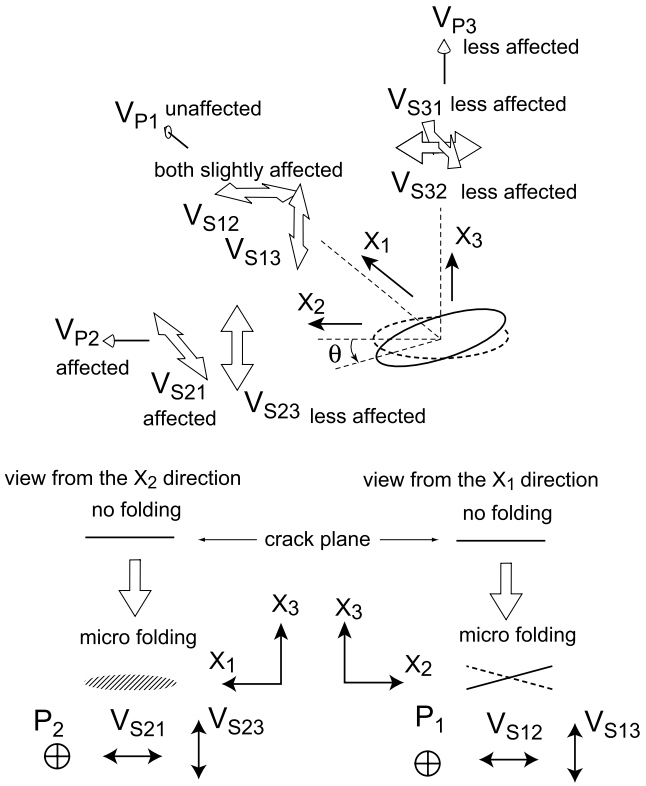

Figure 6. Effect of microfolding on velocities. Microfolding causes tilts of the normals of crack planes and biotite cleavage planes. The tilts affect each velocity in a different way. The most affected velocity is V_{P2} of which ray path is first parallel to crack planes or biotite cleavage planes but is crossing those planes when the tilts appear. V_{P2} then becomes smaller than V_{P1}.

velocity is considerably affected by cracks at the range $0 \leq \theta \leq \pi/4$, but it is little affected at $\pi/4 \leq \theta \leq \pi/2$. This is the reason why $V_{qP}(\pi/4)$ show the smaller velocity increase compared to V_{P3} with decreasing of crack density as shown in Fig. 4. The experimental results on V_{P1}, V_{P3} and $V_{qP}(\pi/4)$ support this, because V_{P3} increases rapidly compared to V_{P1} and $V_{qP}(\pi/4)$ which show almost same velocity increase with respect the confining pressure. $V_{SH}(\pi/4)$ and $V_{qS}(\pi/4)$ come closer to each other as crack density increases, as shown by the thick curves (crack density 0.1) and thin curves (crack-free) in Fig. 7(d). The crossover point of phase velocities is close to the direction $\pi/4$ off from the x_3-axis.

4.5 Crack effects on phase velocities in shale

Shale is one of the important rocks for reservoir assessment and its anisotropy is a much-discussed subject. Shales generally show TI-type anisotropy with strong CPO of clay minerals (Jones & Wang 1981; Hornby *et al.* 1994) accompanying dominant aligned thin microcracks. Clay minerals have strong velocity anisotropy similar to biotite, with large differences between C_{11} and C_{33}, and between C_{44} and C_{66} (Hornby *et al.* 1994). A number of investigations have been done for interpreting velocity anisotropy in shale (Sayers 2002; Hall et al. 2008; Verdon *et al.* 2008). Here we apply our crack model to understand velocity anisotropy of shale under confining pressures or under deviatric stresses.

First, we have to notice the difference between the present metamorphic rock and shale. The matrices of shales are elastically more compliant than the matrices in metamorphic rocks, and elastic compliances of shale matrices change with the confining pressure (Jones & Wang 1981; Hornby *et al.* 1994; Hornby 1998; Sayers 2002; Sarout & Guéguen 2008; Voltolini *et al.* 2009). The velocity increase in shale under confining pressure is not only due to closure of cracks but also due to changes of elastic constants of matrix material by increasing of the contact stiffness between particles under confining pressure. Therefore, it is not easy to extract crack effects only from the velocity data under confining pressures. To interpret the velocity changes in shale under confining pressure, we assume that elastic constants of the matrix is constant and the velocities under confining pressure are only due to closure of cracks. This simple assumption may be useful as the first approximation to understand the wave velocities under confining pressure.

We take the two typical cases of velocities in shale based on the models of Hornby *et al.* (1994): the aligned and the distributed clay-platelet orientations. We assume the bulk modulus of the crack-filled fluid as 0.01 GPa, the case close to gas-filled cracks, which emphasizes crack effects. Figs 8(a-1), (a-2) and Figs 8(b-1), (b-2) show phase velocities for the *qP*, *qS* and *SH* waves. The aligned model shows a remarkable inflection of the V_{qP} distribution curve and a large bulge of the V_{qS} distribution and its diagonal asymmetry in the quadrant. On the other hand, the distributed model shows unclear inflection of the V_{qP} distribution and the small bulge of the *qS* velocity distribution. In both cases, the axial velocity anisotropy defined by Thomsen's parameters ε and γ increases with increasing crack density for both *P* and *S* waves. With increasing crack density, the off-axis bulge in the V_{qS} distribution shrinks. In the quadrant velocity distributions, this moves the crossover point between the *SH* and *qS* waves (singularity) and the maximum value of the *qS*-wave velocity closer to the symmetry axis. Those affect the off-axis shear wave splitting. The polarity of the fast shear wave reverses in some area, and the magnitudes of shear wave splitting increases or decreases depending on the angle θ. For the distributed orientation model, the inflection in the V_{qP} distribution and the singularity of shear waves are not clear. The magnitude of shear wave splitting increases with increasing crack density in the propagation directions $\pi/4 < \theta \leq \pi/2$.

4.6 General characteristics in the TI anisotropy of biotite-rich rocks and shales

As has been shown here, the strong TI anisotropy in biotite-rich rock is characterized by an increase of V_{qS} in the off-axis directions, which is manifested as a bulge and a diagonal asymmetry of the angular distribution of V_{qS}. The magnitude of the off-axis bulge in the V_{qS} distribution is roughly estimated by Thomsen's anisotropic parameter η although it does not reproduce the exact distributions. The angle of the maximum V_{qS} is controlled by θ_m in eq. (23). Table 4 shows a comparison of anisotropy in several TI-type rocks and crack effects on anisotropy. ε, η and θ_m control the characteristics of TI anisotropy such as the shape of the V_{qP} distribution, the magnitude of the bulge in the V_{qS} distribution and the maximum phase-velocity angle in the velocity distributions of *qS* wave. The upper segment of the table shows the effect of cracks and the lower segment shows other shales that have weak anisotropy.

In the upper segment, we assumed $K_f = 0.01$ GPa and crack density (CD) = 0.1 or 0.06. In all the cases, ε increases with increasing crack density. The two typical cases of totally aligned mineral models, biotite-rich rock model I and Cretaceous shale with aligned clay platelet model (Hornby *et al.* 1994), have large η values. The large η indicates increase of V_{qS} in the off-axis directions. With

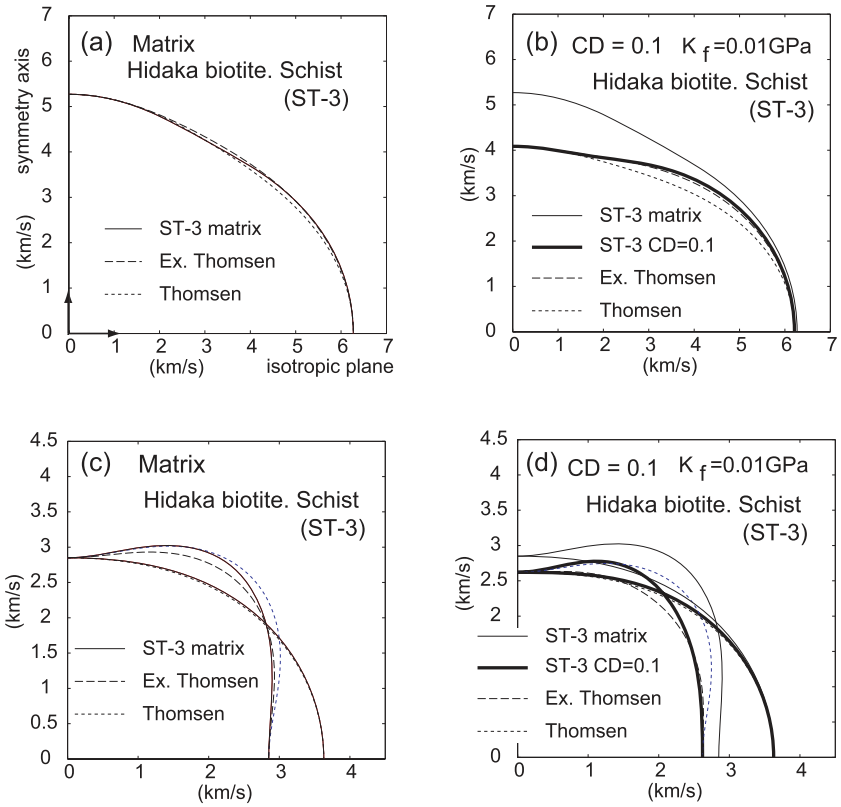

Figure 7. Calculated phase velocity distributions in the x_1x_3- plane of biotite schist (Table 3) for crack-free state and cracked state: (a) crack-free case *qP* wave, (b) cracked case *qP* wave, (c) crack-free case *SH* and *qS* waves and (d) cracked case *SH* and *qS* waves. Crack density is 0.1. Cracks are filled with gas ($K_f = 0.1$ GPa) and their normals align parallel to the TI symmetry axis of biotite schist.

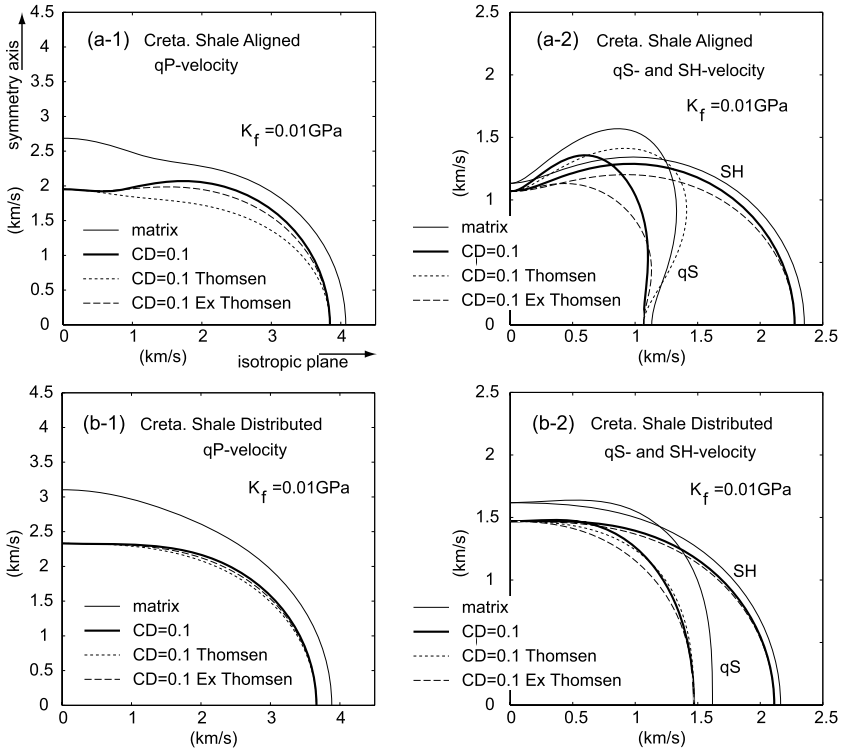

Figure 8. Calculated phase velocity distributions for clay platelets aligned and distributed orientation models for crack density 0.1 and fluid bulk modulus 0.01 GPa. (a-1), (a-2) aligned model. (b-1), (b-2) distributed model.

Table 4. Anisotropic parameters and related parameters of biotite-rich rocks and shale rocks.

Rock	ε	δ_{M}	$\varepsilon - \delta_{\mathrm{M}}$	$\left[\frac{V_P(0)}{V_S(0)}\right]^2$	η	$\theta_m(^\circ)$	ζ_m
Biotite-rich rock model I (matrix)	0.273	−0.254	0.527	5.18	2.732	37.68	0.779
Biotite-rich rock model I (CD=0.06)[a]	0.586	−0.166	0.752	3.91	2.937	31.93	0.785
Hidaka biotite schist	0.208	−0.143	0.351	3.42	1.200	38.43	0.625
Hidaka biotite schist (CD=0.1)[a]	0.648	0.108	0.540	2.43	1.313	29.20	0.573
Creta. shale aligned[(1)]	0.648	−0.131	0.779	5.63	4.384	31.92	0.735
Creta. shale aligned (CD=0.1)[a]	1.364	0.111	1.253	3.48	4.356	24.47	0.728
Creta. shale distributed[(1)]	0.282	0.063	0.219	3.68	0.807	36.89	0.339
Creta. shale distributed (CD=0.1)[a]	0.690	0.391	0.299	2.58	0.773	29.02	0.299
Kaolinite-illite mixture[(4)]	0.766	0.413	0.346	1.89	0.653	25.85	0.346
Kaolinite-illite mixture (CD=0.1)[a]	1.359	1.204	0.155	1.49	0.231	18.23	0.101
Cotton valley shale[(2)]	0.135	0.205	−0.070	2.67	−0.187	36.89	−0.156
Wills point shale[(2)]	0.215	0.315	0.100	7.47	−0.747	39.27	−0.108
Kimmimerridge shale[(3)]	0.344	0.177	0.167	3.47	0.579	35.49	−0.154

[a] $K_{\mathrm{f}} = 0.01$ GPa, [(1)] Hornby *et al.* (1994), [(2)]Berryman (2008), [(3)]Hornby (1998), Voltolini *et al.* (2009), [(4)] Voltolini *et al.* (2009) 100 per cent clay model 50 MPa compression.

increasing the crack density, θ_m decreases, indicating the stronger diagonal asymmetry of the V_{qS} distribution.

With increasing crack density, both Hidaka biotite schist and Cretaceous shale with distributed orientation of clay platelet (Hornby *et al.* 1994) show the same changes in ε and θ_m. If we carefully look into the published experimental data, we find that the off-axis *qS*-wave velocity increases with increasing confining pressure. Sometimes the velocity increase is very small, but it exceeds increases in the *SH*-wave and the axial *S*-wave velocities (Jones & Wang 1981; Hornby 1998; Sarout & Guéguen 2008). This is similar to the increases in V_{qS} in Figs 4(a)–(c). Increase of V_{qS} under confining pressure can be interpreted as an increase of θ_m or extension of the bulge of the V_{qS} distribution with decreasing crack density, as shown in Figs 2, 7 and 8.

It should be noted that θ_m is less than 45° in all cases. Because θ_m is defined by $\tan^2\theta_m = (C_{33} - C_{44})/(C_{11} - C_{44})$, it is less than one because the condition $C_{33} < C_{11}$ always holds in anisotropic sheet silicate-rich rocks. Since cracks reduce *P*-wave velocity along the symmetry axis, C_{33} decreases, $\tan\theta_m$ decreases with increasing crack density and θ_m also decreases. By comparing the values of η, θ_m and ζ_m in the lower segment with those values of the upper segment, we can roughly estimate the behaviour of the *qP*- and *qS*-wave velocity distributions.

4.7 Fitting of the extended Thomsen's approximation

The main point of Berryman's extended Thomsen method is the following approximation for $M(\theta)$ in eq. (12):

$$M(\theta) = \left[(C_{11} - C_{44})\sin^2\theta + (C_{33} - C_{44})\cos^2\theta\right][1 - \zeta(\theta)]^{1/2} \approx \left[(C_{11} - C_{44})\sin^2\theta + (C_{33} - C_{44})\cos^2\theta\right][1 - \zeta(\theta)/2], \tag{26}$$

where $\zeta(\theta)$ is given by

$$\zeta(\theta) = 4\frac{[(C_{11} - C_{44})(C_{33} - C_{44}) - (C_{13} + C_{44})^2]\sin^2\theta\cos^2\theta}{[(C_{11} - C_{44})\sin^2\theta + (C_{33} - C_{44})\cos^2\theta]^2}. \tag{27}$$

The approximation in eq. (26) is valid for small $\zeta(\theta)$. $\zeta(\theta)$ becomes small when θ is close to zero or $\pi/2$. The fitness of the approximation by eq. (26) around the extreme value of $\zeta(\theta)$ is controlled by the magnitude of the extreme value, ζ_m. Values of ζ_m for biotite-rich rock model, Hidaka biotite schist and some shales are listed in Table 4. ζ_m becomes relatively large for strong preferred orientations of biotite or clay platelets. The difference between the approximation and the exact calculation becomes large in the V_{qS} distribution when η is large. η and ζ_m are generally large for a strong anisotropic material like the biotite-rich rock model I and the aligned clay platelet model of the Cretaceous shale. This is the reason why the extended Thomsen's approximation gives poor fits to the exact velocities in those cases. Hidaka biotite schist shows better fits compared to the above rock models for both matrix and cracked cases because of smaller η and ζ_m. For most of the distributed orientation models and natural shale rocks, ζ_m and η are small. In such cases, Berryman's approximation fits well to the exact calculations.

4.8 Shear wave splitting in the off-axis directions

The magnitude of shear wave splitting is measured from the velocity differences between the phase velocities of *SH* and *qS* waves. Shear wave splitting has been used for probing subsurface conditions (Crampin 1987; Crampin, *et al.* 1990). Interpretations based on phase velocities can be applied to teleseismic waves because plane wave assumption is implicitly employed. Here, we tentatively adopt the plane wave assumption and discuss shear wave splitting of phase velocities.

Fig. 9 shows the relative differences between V_{SH} and V_{qS} in per cent, $100 \times (V_{SH} - V_{qS})/[(V_{SH} + V_{qS})/2]$, as functions of θ for Hidaka biotite schist and Cretaceous shale with distributed orientation of clay platelets. The positive area is the normal splitting zone, $V_{SH} > V_{qS}$, whereas the negative area is the reverse, $V_{qS} > V_{SH}$, due to the increase of V_{qS} near the symmetry axis. The boundary of the normal and the reverse zone (zero-crossing) corresponds to the singularity angle. With increasing crack density, the normal zone extends due to the decrease of the off-axis V_{qS} values. Also θ_m decreases. This means that the direction of the extreme value of $M(\theta)$ gets closer to the symmetry axis. In Hidaka biotite schist, increasing of crack density causes an exchange of the fast and slow shear wave polarization near $\theta \lesssim 55^\circ$, where the initial slow-wave polarization direction turns to be the fast-wave polarization direction. The distributed orientation model of Cretaceous shale (Hornby *et al.* 1994) shows a similar trend but the magnitude of shear splitting is smaller.

The relative changes of the shear wave splitting between the crack-free state and the cracked state (crack density 0.1) are

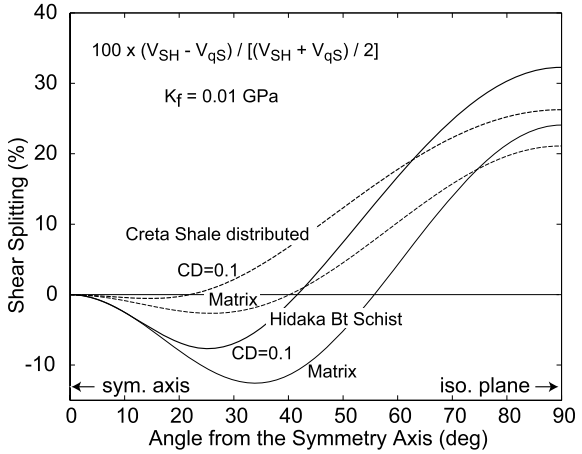

Figure 9. Relative phase velocity differences between two polarized shear waves, V_{SH} and V_{qS}, for Hidaka biotite schist (solid curve) and the distributed model of cretaceous shale (dashed curve) by Hornby *et al.* (1994). The thick and thin curves correspond to the cases of crack density 0.1 and crack-free state (matrix), respectively. Fluid bulk modulus is 0.01 GPa for both cases.

10 per cent for the Hidaka biotite schist and 4 per cent for the distributed orientation model of Cretaceous shale, in the directions $\theta \geq \pi/4$. In the directions $\theta < \pi/4$, the relative changes become smaller and come to zero along the symmetry axis. Observed magnitudes of shear wave splitting depend on the path distances of anisotropic media through which seismic waves propagate. Most of the anisotropic layers will not be thick enough to produce a large traveltime retardation of the two shear waves. However, a sophisticated method presented by Miyazawa *et al.* (2008) observed a 2 per cent shear wave splitting, and suggested that the splitting as small as ∼0.2 per cent can be detected. Considering this, shear wave splitting could be used for monitoring reservoir conditions by observing anisotropy of cap rocks.

5 CONCLUSIONS

Rocks containing large amounts of sheet silicates or clay platelets often show TI-type anisotropy characterized by slow *P*- and *S*-wave velocities along the symmetry axis. This anisotropy is produced by the preferred orientation of sheet silicates or clay platelets. Shear wave anisotropy of such TI-type rocks is mostly characterized by increase of the *qS*-wave velocity (the slow velocity in axial directions) in the off-axis directions with the direction of the maximum value biased to the symmetry axis.

Cracks tend to be formed with their planes parallel to the planes of silicate sheet in sheet silicate minerals. The cracks enhance the existing axial anisotropy caused by CPO of sheet silicate minerals, by reducing the velocities of the *P* and *S* waves along the symmetry axis. Reduction of the *P*-wave velocity along the symmetry axis is closely linked to the change of the off-axis *qS*-wave velocities. An increase of crack density enhances the diagonal asymmetry of the angular distribution of the *qS*-wave velocity, and gives changes in the axial dependence of shear wave splitting between *SH* and *qS* waves. Under certain conditions, a decrease of the off-axis *qS* velocity caused by cracks can appear as exchange of polarization direction between the fast and slow shear waves.

Although biotite schist is not a major constituent of the Earth's crustal rocks, the present results represent a typical case for the most common TI-type rocks, such as shales, in the shallower part of the Earth's crust. Most of the previous measurements on velocity under confining pressure in sheet silicate-bearing rocks could be explained by the aligned crack model. Berryman's formulation for characterizing seismic anisotropy in TI-type rocks can be successfully applied.

Velocity changes due to aligned cracks in TI-type rocks are enhanced when bulk modulus of the crack-filling fluid decreases. For example, gas phase enhances crack effects more than liquid because of the more than three orders of magnitude smaller bulk modulus of gas. The velocity differences between *SH* and *qS* waves are more enhanced in the off-axis directions than in the axial directions in sheet silicate-rich rocks when sheet silicate minerals aligned in the same direction. Anisotropy may be useful for monitoring reservoir cap rocks. Thus this study would present important clues to interpret the mechanism of anisotropy in common TI-type rocks in the shallower part of the Earth.

ACKNOWLEDGMENTS

We wish to thank M. Takanashi and K. Yasunaga for the velocity measurements under confining pressure. R. Kranz kindly reviewed the manuscript and gave the authors some suggestions about crack density and its effect on velocity. The comments from the reviewers were helpful to improve the manuscript.

REFERENCES

Aleksandrov, K.S. & Ryzhova, T.V., 1961. The elastic properties of rock-forming minerals, II: layered silicates, *Izv. Acad. Sci. USSR, Geophys. Ser.,* **12,** 186–189.

Anderson, D., Minster, B. & Cole, D., 1974. The effect of oriented cracks on seismic velocities, *J. geophys. Res.,* **79,** 4011–4015.

Berryman, J.G., 2008. Exact seismic velocities for transversely isotropic media and extended Thomsen formulas for stronger anisotropies, *Geophysics,* **73,** D1–D10.

Barruol, G. & Mainprice, D., 1993. A quantitative evaluation of the contribution of crustal rocks to the shear-wave splitting of teleseismic SKS waves, *Phys. Earth planet. Inter.,* **78,** 281–300.

Burlini, L. & Kunze, K., 2000. Fabric and seismic properties of Carrara marble mylonite, *Phys. Chem. Earth (A),* **25,** 133–139.

Carcione, J.M., 2007. Wave fields in real media: wave propagation in anisotropic, anelastic, porous and electromagnetic media, in *Handbook of Geophysical Exploration I: Seismic Exploration,* Vol. 38, eds Helbig, K. & Treitel, S., Elsevier, Amsterdam.

Chesnokov, E.M., Tiwary, D.T., Bayuk, I.O., Sparkman, M.A. & Brouwn, R.L., 2009. Mathematical modelling of anisotropy of illite-rich shale, *Geophys. J. Int.,* **178,** 1625–1648.

Crampin, S., 1987. Geological and industrial implications of extensive dilatancy anisotropy, *Nature,* **328,** 491–496.

Crampin, S. & Yedlin, M., 1981. Shear-wave singularities of wave propagation in anisotropic media, *J. Geophys.,* **49,** 43–46.

Crampin, S., Boothe, D.C., Evans, R., Peacock, S. & Fletcher, J.B., 1990. Changes in shear wave splitting at Anza near the time of the North Palm Springs earthquake, *J. geophys. Res.,* **95,** 11 197–11 212.

Dellinger, J. & Vernik, L., 1994. Do travel times in pulse-transmission experiments yield anisotropic group or phase velocities? *Geophysics,* **59,** 1774–1779.

Douma, J., 1988. The effect of the aspect ratio on crack-induced anisotropy, *Geophys. Prospect.,* **36,** 614–632.

Eshelby, J.D., 1957. The determination of the elastic field of an ellipsoidal inclusion, and related problems, *Proc. Roy. Soc.,* **A241,** 376–396.

Hall S.A., Kendall, J.M., Maddock, J. & Fisher, Q., 2008. Crack density tensor inversion for analysis of damages in rock frame structure, *Geophys. J. Int.,* **173,** 577–592.

Hill, R., 1952. The elastic behaviour of a crystalline aggregate, *Proc. Phys. Soc., Lond.* **A65,** 349–354.

Hornby, B.E., 1998. Experimental laboratory determination of the dynamic elastic properties of wet, dry shales, *J. geophys. Res.,* **103,** 29 945–29 964.

Hornby, B.E., Schawartz, L.M. & Hudson, J.A., 1994. Anisotropic effective-medium modelling of the elastic properties of shales, *Geophysics,* **59,** 1570–1583.

Hudson, J.A., 1981. Wave speeds and attenuation of elastic waves in material containing cracks, *Geophys. J. R. astr. Soc.,* **64,** 133–150.

Jakobsen, M. & Johansen, T.A., 2000. Anisotropic approximations for mudrocks: a seismic laboratory study, *Geophysics,* **65,** 1711–1725.

Johnston, J.E. & Christensen, N.I., 1994. Elastic constants and velocity surfaces of indurated anisotorpic shales, *Surv. Geophys.,* **15,** 481–494.

Jones, L.E.A. & Wang, H.F., 1981. Ultrasonic velocities in Creataceous shales from the Williston basin, *Geophysics,* **46,** 288–297.

Kendall, J.-M. *et al.*, 2007. Seismic anisotropy as an indicator of reservoir quality in siliciclastic rocks, in *Structurally Complex Reservoirs,* Vol. 292, pp. 123–136, eds Jolley, S., Barr, D., Walsh, J. & Knipe, R.J., Geological Society, Special Publications, London.

Kern, H., 1993. P- and S-wave anisotropy and shear-wave splitting at pressure and temperature in possible mantle rocks and their relation to the rock fabric, *Phys. Earth planet. Inter.,* **78,** 245–256.

Kern, H. & Wenk, H.-R., 1990. Fabric-related velocity anisotropy and shear wave splitting in rocks from the Santa Rosa mylonite zone, California, *J. geophys. Res.,* **95,** 11 213–11 223.

Landau, L.D. & Lifshitz, E.M., 1959. *Theory of Elasticity,* Pergamon, Oxford, (3rd edition in 1985, Butterworth-Heinemann).

Le Ravalec, M. & Guéguen, Y., 1996a. High and low frequency elastic moduli for a saturated porous/cracked rock (differential self consistent and poroelastic theories), *Geophysics,* **61,** 1080–1094.

Le Ravalec, M. & Guéguen, Y., 1996b. Comments on "The elastic modulus of media containing strongly interacting cracks" by Paul M. Davis and Leon Knopoff, *J. geophys. Res.,* **101,** 25 373–25 375.

Lin, S. & Mura, T., 1973. Elastic fields of inclusions in anisotropic media (II), *Phys. Status Solidi, A,* **15,** 281–285.

Markov, M., Levine, V., Mousatov, A. & Kazatchenko, E., 2005. Elastic properties of double-porosity rocks using the differential effective medium model, *Geophys. Prospect.,* **53,** 733–754.

Mavko, G., Mukerji, T. & Dvorkin, J., 1998. *The Rock Physics Handbook: Tools for Seismic Analysis in Porous Media,* Cambridge University Press, Cambridge.

Miyazawa, M., Snieder, R. & Venkataraman, A., 2008. Application of seismic interferometry to extract P- and S-wave propagation and observation of shear-wave splitting from noise data at Cold Lake, Alberta, Canada, *Geophysics,* **73,** D35–D40.

Mura, T., 1982. *Micromechanics of Defects in Solids,* Martinus Nijhoff Publishers, Hague.

Nishizawa, O., 1982. Seismic velocity anisotropy in a medium containing oriented cracks-transversely isotropic case, *J. Phys. Earth,* **30,** 331–347.

Nishizawa, O. & Yoshino, T., 2001. Seismic velocity anisotropy in mica-rich rocks: an inclusion model, *Geophys. J. Int.,* **145,** 19–32.

Nur, A. & Simmons, N., 1969. The effect of saturation on velocity in low porosity rocks, *Earth planet. Sci. Lett.,* **7,** 183–193.

O'Connell, R.J. & Budiansky, B., 1974. Seismic velocities in dry and saturated solids, *J. geophys. Res.,* **79,** 5412–5426.

Pros, Z, Lokajíček, T., Přkryl, R., Špičák, A, Vajdová, V. & Klíma, K., 1998. Elastic parameters of West Bohemian granites under hydrostatic pressure, *Pure appl. Geophys.,* **151,** 631–646.

Sarout, J. & Guéguen, Y., 2008. Anisotropy of elastic wave velocities in deformed shales. Part 1—experimental results, *Geophysics,* **73,** D75–D89.

Sayers, C.M., 2002. Stress-dependent elastic anisotropy of sandstones, *Geophys. Prospect.,* **50,** 85–95.

Simmons, G., Siegfried, R. & Feves, M., 1974. Differential strain analysis: a new method for examining cracks in rocks, *J. geophys. Res.,* **79,** 4383–4385.

Soga, N., Mizutani, H., Spetzler, H. & Martin, R.J., 1978. The effect of dilatancy on velocity anisotropy in Westerly granite, *J. geophys. Res.,* **83,** 4451–4456.

Takanashi, M., Nishizawa, O., Kanagawa, K. & Yasunaga, K., 2001. Laboratory measurements of elastic anisotropy parameters for the exposed crustal rocks from Hidaka metamorphic belt, central Hokkaido, Japan, *Geophys. J. Int.,* **145,** 33–47.

Thomsen, L., 1986. Weak elastic anisotropy, *Geophysics,* **51,** 1954–1966.

Tsvankin, I., 1997. Anisotropic parameters and *P*-wave velocity for orthorhombic media, *Geophysics,* **62,** 1292–1300.

Vaughan, M.T. & Guggenheim, S., 1986, Elasticity of muscovite and its relationship to crystal structure, *J. geophys. Res.,* **91,** 4657–4664.

Vavryčuk, V., 2003. Parabolic lines and caustics in homogeneous weakly anisotropic solids, *Geophys. J. Int.,* **152,** 318–334.

Verdon, J.P., Angus, D.A., Kendall, J.M. & Hall, S.A., 2008. The effect of microstrucuter and nonlinear stress on anisotropic seismic velocities, *Geophysics,* **73,** D41–D51.

Voltolini, M., Wenk, H.-R., Mondol, N.H., nut Bjorlykke, K. & Jahren, J., 2009. Anisotropy of experimentally compressed kaolinite-illite-quartz mixtures, *Geophysics,* **74,** D13–D23.

Walsh, J.B., 1965. The effect of cracks on the compressibility of rock, *J. geophys. Res.,* **9,** 381–389.

Wang, Z., 2002. Seismic anisotropy in sedimentary rocks, part 2: laboratory data, *Geophysics* **67,** 1423–1440.

Yamamoto, K., Kosuga, M. & Hirasawa, T., 1981. A theoretical method for determination of effective elastic constants of isotropic composite, *Sci. Rep. Tohoku Univ., Ser. 5,* **28,** 47–67.